Failure analysis of CFRP laminates subjected to Compression After Impact: FE simulation using discrete interface elements

Samuel Rivallant, Christophe Bouvet, Natthawat Hongkarnjanakul

Failure analysis of CFRP laminates subjected to compression after impact: FE simulation using discrete interface elements

Samuel Rivallant, Christophe Bouvet *, Natthawat Hongkarnjanakul

Université de Toulouse, INSA, UPS, Mines Albi, ISAE, ICA (Institut Clément Ader) ISAE (Institut Supérieur de l'Aéronautique et de l'Espace), 10 Avenue Edouard Belin – BP54032, 31055 Toulouse CEDEX 4, France

ARTICLE INFO

Keywords:
Composite
Impact damage
CAI
Damage tolerance

ABSTRACT

This paper presents a model for the numerical simulation of impact damage, permanent indentation and compression after impact (CAI) in CFRP laminates. The same model is used for the formation of damage developing during both low-velocity/low-energy impact tests and CAI tests. The different impact and CAI elementary damage types are taken into account, i.e. matrix cracking, fiber failure and interface delamination. Experimental tests and model results are compared, and this comparison is used to highlight the laminate failure scenario during residual compression tests. Finally, the impact energy effect on the residual strength is evaluated and compared to experimental results.

1. Introduction

Over the past decades, composite materials have been increasingly introduced in aircraft structures and space applications because of their interesting characteristics, like their low specific weight, enhanced mechanical strength and high stiffness. Nevertheless, one of the main disadvantages of composite materials is damage induced during the structure's life by impacts of small and large objects, like hailstones, runway debris or falling tools, that can drastically decrease the structure's strength.

One of the most critical loading for composite laminates is low-velocity impact. Indeed, for structures submitted to low-energy impacts or small object drops, like tools during assembly or maintenance operations, composite laminates show brittle behavior and can undergo significant damage in terms of matrix cracks, fiber breakage or delamination. This damage is particularly dangerous because it drastically reduces the residual mechanical characteristics of the structure, and, at the same time, can leave a very small visible mark on the impacted surface [1], which makes it difficult to detect.

It is therefore essential to define a damage tolerance demonstration to design this type of structure in such a way that the possible damage is taken into account. In the field of aeronautics, damage tolerance, for damage corresponding to impact loading, is used to size the structure according to the impact detectability [2]. If the damage is not detectable, i.e. when the impact indentation is less than barely visible impact damage (BVID), the structure must support the extreme loads; if the damage is detectable, i.e. when the impact indentation is bigger than BVID, another criterion must be considered, like repair or change of the structure [3,4].

In order to reduce both the time and cost of development, we can imagine the use of virtual tools to numerically optimize a composite structure with the impact damage tolerance concept. It is then necessary to simulate the impact damage, and in particular the permanent indentation, and use the results of impact simulation (damage mapping, deformed shape, etc.) to simulate the CAI test in order to evaluate the residual strength versus impact energy and permanent indentation. This is the scope of the proposed study which shows the ability to simulate both impact and residual strength tests within the same model.

A significant number of studies about the impact behavior of composite laminates are available in the literature, both experimentally [1,5,6] and numerically [1,7,8]. There are fewer experiments on residual strength or CAI tests, and very few works concerning the prediction of residual strength using models. These models can be based on analytical approaches [9,10], semi-empirical approaches [11] or FE calculations [12–17]; we can also cite some works conducted on sandwiches [18,19]. Most of these works are only based on delamination growth and/or sublaminate buckling instability criteria for strength prediction, which can be a great limitation as in some cases where the presence of damage, such as fiber failure cracks around the impact area, seems to be the key to final rupture during CAI tests.

* Corresponding author.
E-mail addresses: samuel.rivallant@isae.fr (S. Rivallant), christophe.bouvet@isae.fr (C. Bouvet).

This said, some authors present more complex methods, like Soutis et al. [14,16] who proposed an original model, inspired by the analogy in failure mechanisms between CAI and compression of open holes. This model seems to give good results, but essentially in the case of cylindrical impact damage. Yan [17] also uses a complex FE simulation, with modeling of some damage propagation in the fabric laminate during CAI. In spite of that, all the above-mentioned works are severely limited due to the fact that the damage used for the CAI calculation is not predicted, but simply implemented in the model using experimental observations such as permanent indentation shape or non-destructive control method which limits the application range of these models. One solution would be to have a model that can predict the damage due to impact, and then simulate the CAI test.

To the author's knowledge, there are very few studies in the literature about models for both impact and CAI testing. There are two about sandwich structures: the first one is the work done by Davies [20] on composite sandwiches, but contrary to the above-mentioned models, it accounts for fiber failures, core crushing, but not delamination in skin and debonding between the core and skins. The second one, by Aminanda [21], deals with impacts on sandwiches with metallic skin, and focuses on the behavior of the core. Concerning composite laminates, the recent study by González [22] proposes the use of the same 3D FE model with intralaminar (fiber and matrix) and interlaminar damage, both for impact and CAI test simulation. Impact calculations well match the experimental curves, except for some of the experiment data. Moreover, CAI strength values are consistent during tests and simulations (less than 20% difference), even if the author only gives final rupture values but not the force–displacement curves. We can also mention Falzon's works [23] on CAI modeling for stiffened panels.

This research paper is a complementary work from Bouvet et al. [24] who have developed an impact FE model, aiming to model impact damage and permanent indentation. This model is improved and used to simulate the CAI test; the fiber failure criterion under compression loading, which is of utmost importance during CAI testing, has been modified. Finally, this model is compared with experimental results of CAI tests with different impact energies. It enables the global simulation of impact damage, such as delaminated areas, fiber failure or permanent indentation, and the CAI damage, like fiber failure propagation or local buckling of delaminated areas.

2. Numerical modeling

In previous studies, Bouvet et al. [24–26] presented a discrete 3D FE model of impact on laminated composites. The model is simulated in explicit/dynamic response in Abaqus with a subroutine Vumat. According to experimental observation, impact damage can be modeled separately in (i) fiber failure within 3D elements, (ii) intra-ply matrix cracking with cohesive elements and (iii) delamination in between plies also with cohesive elements (Fig. 1a). These types of damage are coupled with a specific mesh construction, oriented at 0°, 90°, 45° and −45° (Fig. 1b). Positions of nodes are uniformly stacked in rows and columns for all ply orientations but mesh shapes are different: 0° and 90° plies are meshed with square elements, while 45° and −45° plies are meshed with parallelogram elements to follow the fiber direction, and so that nodes in neighboring plies coincide. In this study, the size of elements in 0° and 90° plies are around $1.4 \times 1.4 \times 0.5\ \text{mm}^3$, where 0.5 mm is the thickness. Only half of the plate is modeled, due to symmetry considerations (central symmetry around the z axis), using kinematic relations between symmetric nodes of the (xz) plane.

This model is completed to enable CAI modeling with the same model as for impact simulation. Observations of mechanisms involved in CAI, and in particular the existence and propagation of cracks due to fiber failure in compression, led to the improvement of the fiber failure law.

2.1. Fiber failure modeling

Fiber failure is taken into account using a failure criterion written inside the volume elements. This criterion is based on fracture mechanics in order to be able to dissipate the critical energy release rate in opening mode (mode I) due to fiber fracture (Fig. 1a) in the volume elements. It is an extension of the fiber failure model presented in [24], which is limited to failure in tension.

During the elastic part of the behavior law, strains in the volume elements are calculated at the 8 Gauss points (ε^i), and extrapolated to the 8 nodes (ε^{node}), in order to take into account the strain due to ply bending at damage initiation. When any of the eight strains calculated at the nodes reaches the failure strain in tension (ε_0^T) or in compression (ε_0^C) (Eqs. (1) and (2)), all stresses at the eight integration points are simultaneously established in the damage initiation state at $t = t_0$, as illustrated in Fig. 2b.

$$\max_{\text{node}=1}^{8} (\varepsilon^{\text{node}}) \geqslant \varepsilon_0^T \tag{1}$$

$$\min_{\text{node}=1}^{8} (\varepsilon^{\text{node}}) \leqslant \varepsilon_0^C \tag{2}$$

Then, for the propagation of damage, a simplified formulation is used to dissipate the constant energy release rate per unit area in the 3D continuum element, based on the crack band theory from Bazant [27]. It can be written as:

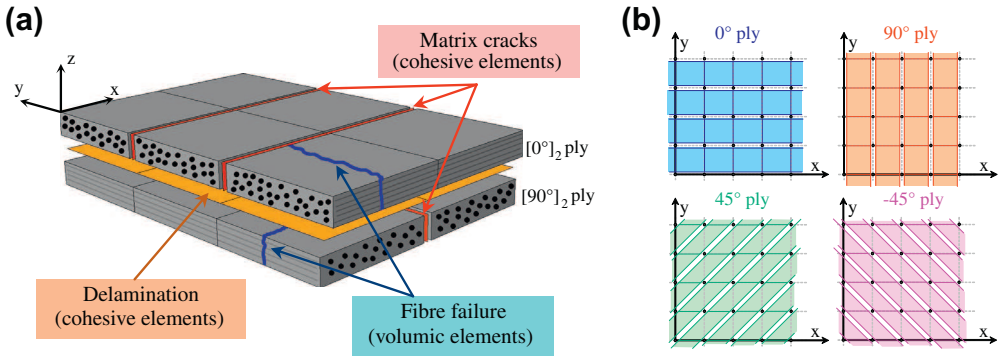

Fig. 1. (a) Impact damage model and associated element types and (b) Mesh shape for each ply orientation. (For interpretation of the references to color in this figure legend, the reader is referred to the web version of this article.)

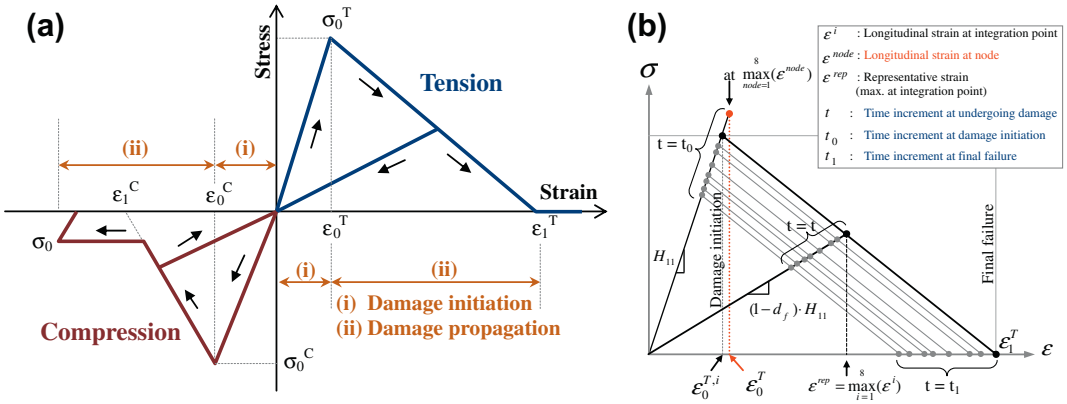

Fig. 2. (a) Fiber failure behavior law in longitudinal direction and (b) Detail of the law applied to a 3D element in tension. (For interpretation of the references to color in this figure legend, the reader is referred to the web version of this article.)

$$\int_V \left(\int_0^{\varepsilon_1} \sigma \cdot \mathrm{d}\varepsilon \right) \cdot \mathrm{d}V = S \cdot G_I^f \tag{3}$$

where $\left(G_I^f\right)$, ε, and ε_1 are respectively the fracture toughness for the opening mode (I), the strain in fiber direction, and the strain in fiber direction at final failure. As seen in Fig. 2a, these parameters are applicable either in tension ($G_I^f = G_I^T$ and $\varepsilon_1 = \varepsilon_1^T$), or in compression ($G_I^f = G_I^C$ and $\varepsilon_1 = \varepsilon_1^T$). V and S are the element's volume and cross section normal to fiber direction, respectively. Then, V and S can be reduced in terms of an internal element length l, which is comparable to the FE characteristic length used in [27,28] to make FE model mesh size independent. Note that the superscripts 0 and 1 denote damage initiation and final failure, respectively.

In addition to distributing the fracture energy over the whole volume element, Bouvet et al. [24] have proposed a new approach to dissipate this energy, defined in terms of the eight integration points of each volume element, shown in Fig. 2b. In order to manage damage propagation, the representative strain $\varepsilon^{\mathrm{rep}}$ is defined as the maximum strain of the eight integration points, and is computed at each time increment:

in tension:

$$\varepsilon^{\mathrm{rep}} = \max_{i=1}^{8}(\varepsilon^i) \tag{4}$$

in compression:

$$\varepsilon^{\mathrm{rep}} = \min_{i=1}^{8}(\varepsilon^i) \tag{5}$$

The behavior laws at the 8 Gauss points of a volume element are driven together to dissipate the same energy as the critical energy release rate in mode I of a plane crack normal to the fiber direction through the element. The tensile or compression final failure strain (ε_1^T or ε_1^C) can then be determined by solving Eq. (3). At each time increment, ε_1^T (or ε_1^C) and $\varepsilon^{\mathrm{rep}}$ are updated during the damage propagation state in progress; the linear degradation of strain-softening can be assigned in terms of the damage variable d_f defined in Eqs. (6) and (7).

in tension:

$$d_f = \frac{\varepsilon_1^T\left(\varepsilon^{\mathrm{rep}} - \varepsilon_0^{T,i}\right)}{\varepsilon^{\mathrm{rep}}\left(\varepsilon_1^T - \varepsilon_0^{T,i}\right)} \tag{6}$$

in compression:

$$d_f = \frac{\varepsilon_1^C\left(\varepsilon^{\mathrm{rep}} - \varepsilon_0^{C,i}\right)}{\varepsilon^{\mathrm{rep}}\left(\varepsilon_1^C - \varepsilon_0^{C,i}\right)} \tag{7}$$

where $\varepsilon_0^{T,i}$ (or $\varepsilon_0^{C,i}$) is the tensile strain at damage initiation, translated to the integration point in order to take into account d_f at the integration points instead of the nodes. Note that the damage variable d_f, which is computed using the representative strain, is the same for the 8 Gauss points and governs the linear degradation behavior, as illustrated in Fig. 2b.

Due to the complexity of the damage propagation state in compression, the energy release rate for compression is very difficult to evaluate and even the meaning of this value is very complex and seems to correspond to the initiation value but not to propagation. In fact, for this modeling, the propagation value is needed; to overcome this problem, an artificially low value (Table 1) was adopted in order to prevent this phenomenon dissipating too much energy. This point is being studied and should be confirmed with other experimental tests inducing compression fiber failure.

Furthermore, the fiber compressive failure behavior is slightly more complicated than in tension. Crack initiation in compression is due to kink band with the associated dissipated energy, as mentioned by Pinho [29], but when one continues to apply compression, the two sides of the crack come into contact and lead to the crushing of packs of fibers. Therefore, a compressive mean crushing stress (σ_0), as defined by Israr et al. [30], is applied as a plateau to complete the law, as can also be seen in the works by Faggiani [31]. Moreover, during the plateau, plasticity is also taken into account to prevent compressive strain from returning to zero during the unloaded state, as illustrated in Fig. 2a.

Then, using elastic properties given in Table 1, both in tension or in compression, the stiffness matrix $[H]$ can be written as:

$$\begin{Bmatrix} \sigma_{11} \\ \sigma_{22} \\ \sigma_{33} \\ \sigma_{12} \\ \sigma_{13} \\ \sigma_{23} \end{Bmatrix} = \begin{vmatrix} (1-d_f)H_{11} & (1-d_f)H_{12} & (1-d_f)H_{13} & 0 & 0 & 0 \\ & H_{22} & H_{23} & 0 & 0 & 0 \\ & & H_{33} & 0 & 0 & 0 \\ & & & (1-d_f)H_{44} & 0 & 0 \\ & \text{sym} & & & (1-d_f)H_{55} & 0 \\ & & & & & (1-d_f)H_{66} \end{vmatrix} \begin{Bmatrix} \varepsilon_{11} \\ \varepsilon_{22} \\ \varepsilon_{33} \\ \varepsilon_{12} \\ \varepsilon_{13} \\ \varepsilon_{23} \end{Bmatrix} \tag{8}$$

2.2. Matrix cracking modeling

A particular meshing of matrix cracking in between neighboring volume elements is introduced with the use of zero-thickness 3D

Table 1
Material properties of T700/M21 for numerical simulation.

E_l^t (GPa)	E_l^c (GPa)	E_t (GPa)	ν_{lt}	G_{lt} (GPa)	σ_t^f (MPa)	τ_{lt}^f (MPa)	G_I^d (N/mm)	G_{II}^d (N/mm)	ε_0^t	ε_0^c	G_I^t (N/mm)	G_I^c (N/mm)	σ_0 (MPa)	ε_t^0	k_t (MPa/mm)	ρ (kg/m^3)
130	100	7.7	0.3	4.8	60	110	0.5	1.6	0.016	-0.0125	133	10	−200	0.02	10,000	1600

cohesive elements (interface elements) in the fiber direction (Fig. 1). The classic quadratic criterion of matrix cracking is then applied to these volume elements. As soon as this criterion is reached in either one or both neighboring volume elements, the information is transferred to the cohesive element thanks to a specific element connectivity table and external variables. The transverse stress in cohesive elements and its stiffness are then set to zero, meaning that the matrix is broken with elastic brittle behavior. For this type of damage, the material parameters (Table 1) are the matrix transverse failure σ_t^f and the shear failure stress τ_{lt}^f.

The authors do not think that it is necessary to represent the complex matrix microcrack network but only stripes of plies that enable the simulation of the changes in load transfers between parts of plies when the matrix is damaged, and therefore the occurrence of delamination and fiber failures. A very fine mesh is therefore not necessary. For the same reason, the energy dissipated in matrix cracking is not taken into account in the interface model (brittle failure). It is nevertheless included in the energy dissipated in the delamination interfaces to keep the energy balance. The proof of the relevance of this modeling type has already been shown in previous works of the authors [24], and in the literature [32].

These matrix crack interface elements are also used to simulate permanent indentation.

Some authors assume that permanent indentation is mostly due to plasticity in composites, and therefore need a plasticity-based approach like in [33] or [34]. Experimental observations made in a previous work by Abi Abdallah et al. [35] show that permanent indentation seems to be mainly due to blocking by impact debris; this phenomenon was taken into account in the proposed model. In order to do this, a "like-plasticity" model [24] was introduced in the matrix cracking interfaces in order to limit their closure after failure in tension (σ_t) and in out-of-plane shear (τ_{tz}) directions. Consequently, two additional material parameters, ε_t^0 the dimensionless size of debris and k_t its stiffness, are needed to take into account the phenomenon of permanent indentation. These 2 parameters are difficult to associate with traditional material parameters evaluated during traditional tests and are in fact directly evaluated thanks to a reference impact test. This evaluation process limits the predictive character of this model, in particular for the part linked to permanent indentation. Other works are currently in progress to evaluate these parameters with other, simpler experimental investigations.

2.3. Delamination modeling

Delamination, formed between different orientation plies, is normally taken into account thanks to interface elements based on fracture mechanics (Fig. 3). Zero-thickness 3D cohesive elements join lower and upper ply volume elements. The initiation of delamination is based on a quadratic criterion, similar to that of matrix cracking, and its propagation in a linear coupling in 3 modes (Fig. 3). Mode I (opening) is in the thickness direction normal to the delamination plane, while modes II and III are assumed to be equal, in the in-plane directions. The value of stiffness for the interface is chosen very high (10^6 MPa/mm). Stress values for initiation are the same as for matrix cracking (Table 1). Two additional material parameters are then needed, the critical energy release rate for delamination propagation in mode I $\left(G_I^d\right)$ and in mode II $\left(G_{II}^d\right)$.

3. Experimental validation of modeling

Impact tests were performed in a drop tower system with a 2 kg – 16 mm diameter impactor, as per Airbus Industries Test Method (AITM 1–0010) [36]. The specimens tested were 100 × 150 × 4.16 mm^3 rectangular plates simply supported by a boundary condition of a 75 × 125 mm^2 window. The laminated plate is manufactured with 0.26 mm thick T700/M21 unidirectional carbon/epoxy plies, with stacking sequence $[0_2,45_2,90_2,-45_2]_{sym}$. This stacking sequence was chosen in order to reduce computational time by using double plies during the development of the model. The authors assume that mechanisms leading to the final rupture of the plate in CAI are the same whatever the ply thickness and orientation within a relatively wide range: the combination of bending stress due to buckling and compressive stress concentration leading to fiber failure, as mentioned in a number of recent experimental works [37–40].

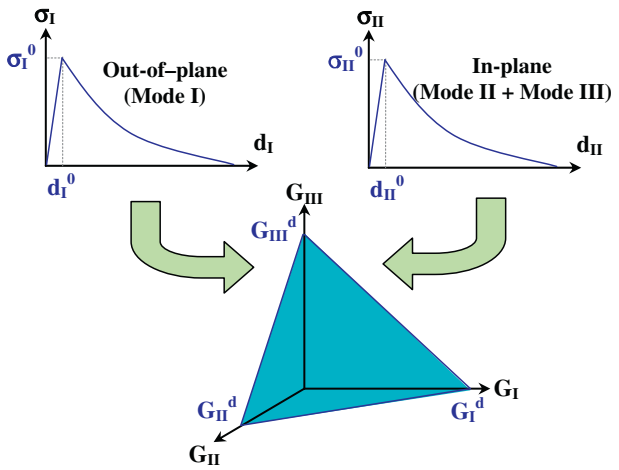

Fig. 3. Delamination in modes I, II and III and linear coupling fracture in 3 modes. (For interpretation of the references to color in this figure legend, the reader is referred to the web version of this article.)

CAI tests were then performed on a hydraulic machine, the specimen being stabilized by a 90 × 130 mm^2 window, as per Airbus Industries Test Method (AITM 1-0010) [36].

The composite plates were tested experimentally and numerically, at 1.6, 6.5, 17, 26.5 and 29.5 J of impact energy, and the corresponding CAI tests were performed. The simulation was performed in three steps (Fig. 4). The first step corresponds to the impact test, with the plate simply supported by a 75 × 125 mm^2 window. This step lasted about 5 ms. At the end of this step, the impact damage was obtained, in particular permanent indentation. The second step consists in the stabilization of oscillations due to impact and the modification of the boundary conditions to set up those of CAI: the knife edges and grips were introduced and progressively moved towards the plate like in experimental tests. Finally, the third step consists in the CAI step, with an imposed displacement of one grip until the final fracture of the plate. As the model was simulated using an explicit code, the grip displacement speed was chosen at 3.75 m/min to reduce CPU time. It is far greater than the experimental value, but a study on the influence of this speed on the CAI simulation results showed the relevance of the choice. The total calculation time of this model is between 12 and 15 h – depending on the impact energy level – with 8 CPUs and without optimization of the modeling to decrease this time.

3.1. Numerical and experimental comparison of impact tests

The comparison between the delamination areas and the force–displacement curves obtained numerically and experimentally are shown in Fig. 5. It should be noted in this figure that an experimental problem did not allow us to obtain the 17 J curve. Globally, the fact

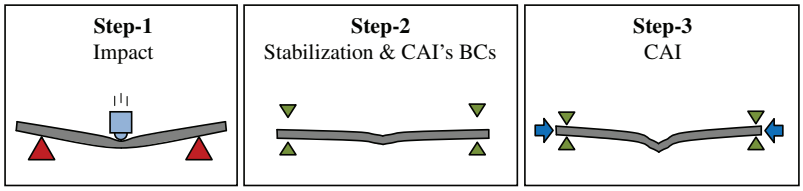

Fig. 4. The three steps of the simulation. (For interpretation of the references to color in this figure legend, the reader is referred to the web version of this article.)

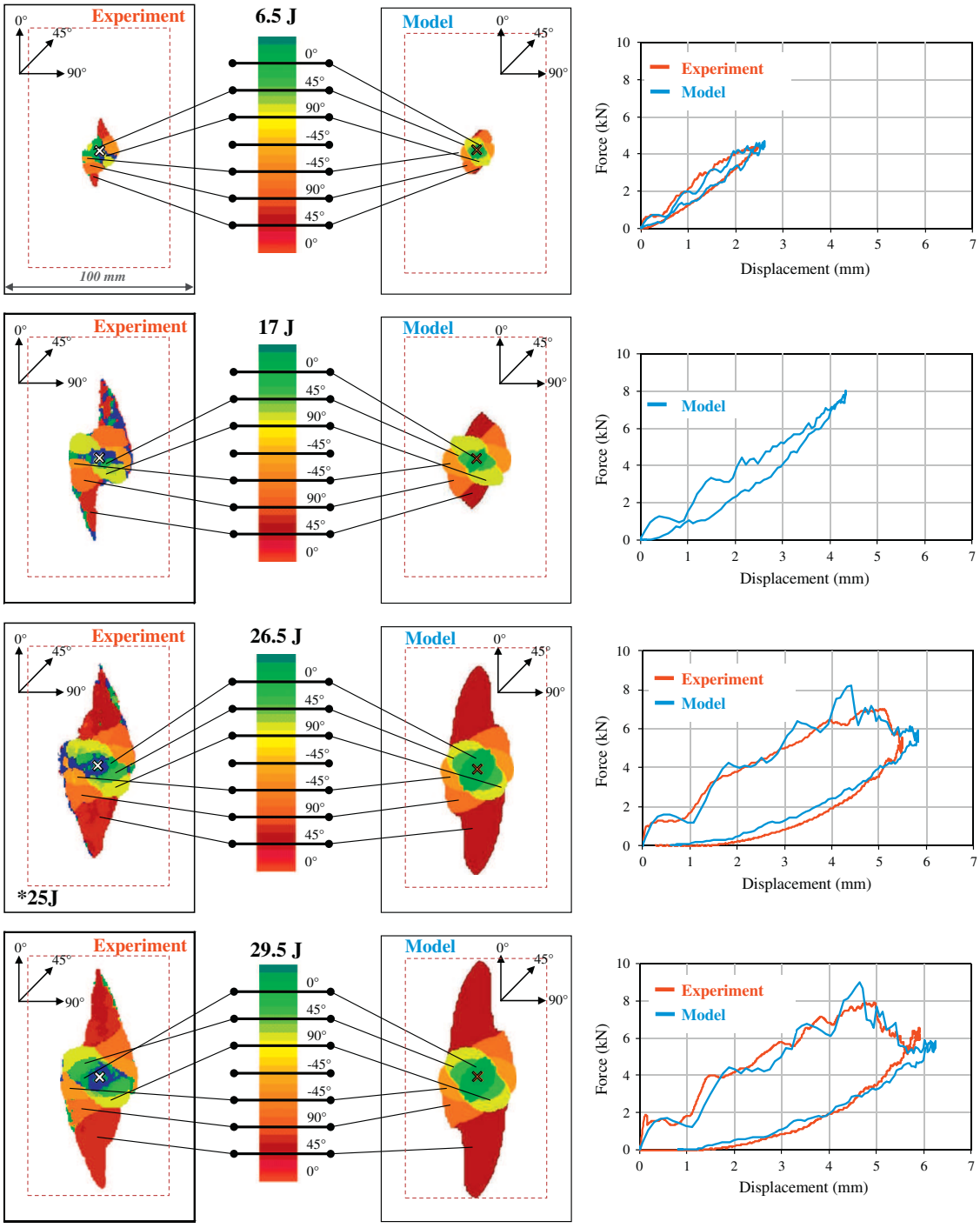

Fig. 5. Delamination areas and force–displacement curves of impact tests. (For interpretation of the references to color in this figure legend, the reader is referred to the web version of this article.)

of taking into account the rupture in compression in the fiber law does not significantly change the results on the curves and damage compared to results previously presented ([24,25]). In the whole range of energies considered, a relatively good correlation is observed between modeling and experiments; the shape and size of the delaminated interfaces are well simulated (Figs. 5 and 6), even if the area of the first interface, non-impacted side, is overestimated for the highest energies. The simulated force–displacement curves take into account the different stiffness decreases: the first one at about 2 mm-displacement is soft and mainly due to delamination, and the second one, at about 5 mm-displacement, is strong and mainly due to fiber failure. Permanent indentation is also well represented (Fig. 6); this highlights the relevance of the "like-plasticity" model used for matrix crack closure.

Even if the new law for fiber failure in compression does not lead to significant differences in the global behavior of the plate (curves and delamination areas), it enables the presence of compression cracks, as can be observed after 29.5 J impact simulation in the central zone under the impactor (Fig. 7), to be taken into account. It can be noticed in Fig. 7 that only the half-plate is drawn and that the deformed shape is free of exterior loads and then only due to the "like-plasticity" model in the matrix cracking elements mentioned above. Most fiber failures are due to tension failures and only the zone just under the impactor, impacted side, presents some compression failures. However, a fiber failure crack in compression is also observed on the impacted side right next to the point of impact (Fig. 7). This crack only concerns the first 0° ply, impacted side. Of course, due to the symmetry of the modeling, this crack exists "virtually" on the other half-plate. This crack turns out to be of utmost importance during CAI because its propagation induces the final fracture of the plate. In fact, after impact tests, this crack is not so obvious on the specimens and is therefore slightly overestimated by the modeling. Unfortunately, as we did not look for cracks after impact tests, it is not possible to prove their presence on the specimen that we tested in CAI, but Fig. 8 shows cracks after two different static indentation tests. Fig. 8a is a microscopic observation of a barely visible crack (not a compression crack, but one which can propagate in compression during CAI) due to a 24.8 J static indentation, whereas Fig. 8b clearly shows the visible compression cracks due to a slightly higher

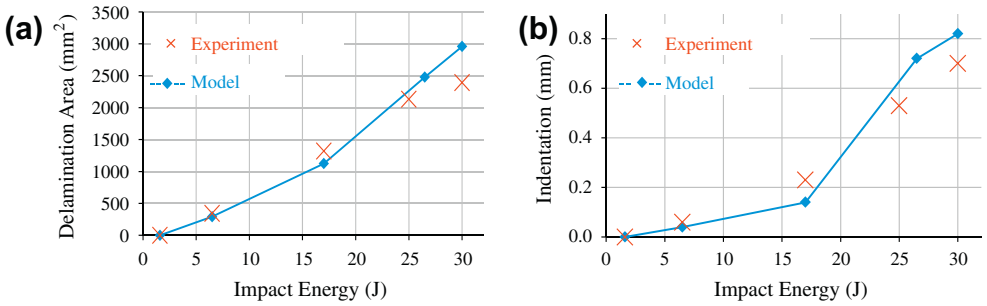

Fig. 6. Delamination area (a) and Permanent indentation (b) as a function of impact energy. (For interpretation of the references to color in this figure legend, the reader is referred to the web version of this article.)

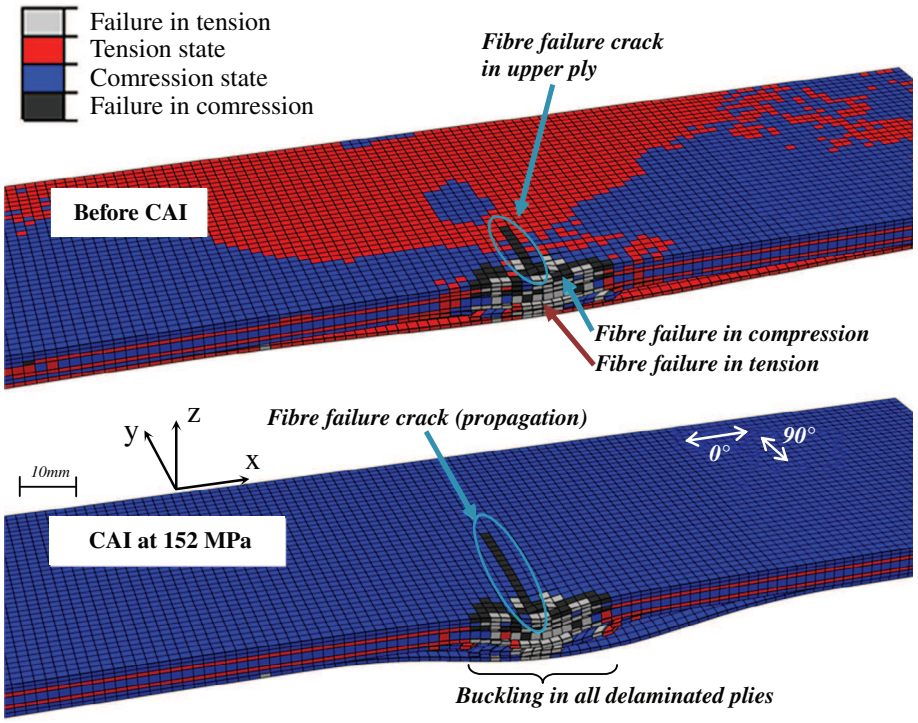

Fig. 7. Fiber failures in the 29.5 J impact test plate: before CAI / During CAI. (For interpretation of the references to color in this figure legend, the reader is referred to the web version of this article.)

energy: 27.3 J static indentation. For lower impact energies, it seems that the latter crack is not visible after impact on the surface of the plate.

3.2. Numerical and experimental comparison of CAI tests

The experimental stress/displacement and stress/deflection curves for 6.5, 17 and 29.5 J impact tests are shown in Fig. 9. For the 17 J test, the buckling shape obtained is in the opposite direction compared to the other tests, which cannot be predicted by the model. In order to have more results to present, a static test at 17 J, performed during another test campaign, is added. It is a static indentation test performed with a universal testing machine at the speed of 0.5 mm/min for both loading and unloading. The hemispherical indenter and the boundary conditions imposed on the plate are the same as during impact tests.

The stress-displacement curve corresponds to the curve of the mean stress, evaluated by dividing the load force by the section, as a function of the longitudinal displacement, in the 0° direction, imposed during CAI testing. These curves show that the model correctly represents the global behavior of the plate until rupture for various impact energy levels: very good match for the slope and

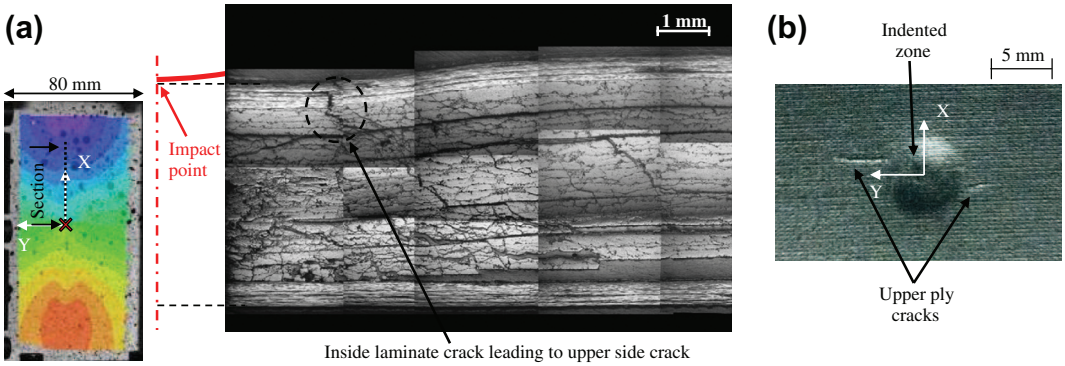

Fig. 8. Cracks initiated by static indentation: (a) static indentation at 24.8 J: barely visible crack (microscope) and (b) static indentation at 27.3 J: visible cracks (photo). (For interpretation of the references to color in this figure legend, the reader is referred to the web version of this article.)

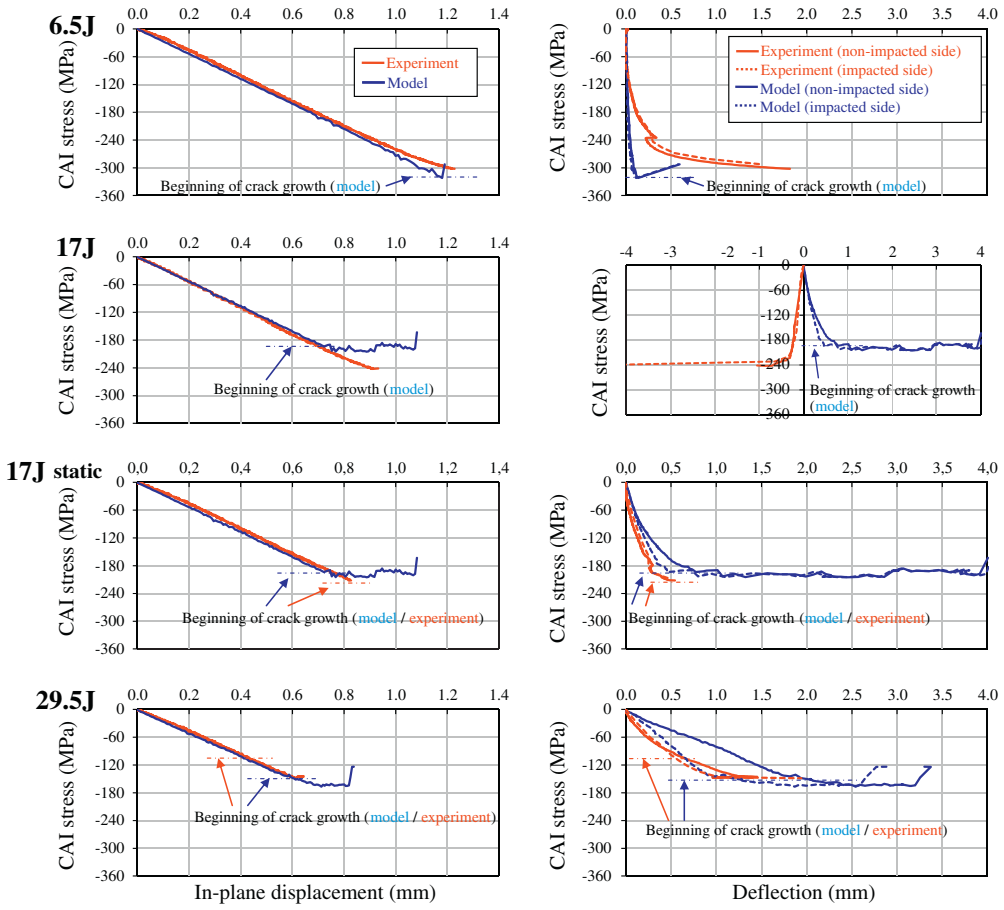

Fig. 9. CAI stress versus in-plane displacement (left) and deflection (right) for three impact energy levels. (For interpretation of the references to color in this figure legend, the reader is referred to the web version of this article.)

good match for the final failure load. Fig. 10a represents the CAI stress versus impact energy for all the tested laminates, which confirm the consistency between experimental and numerical data: less than 20% difference in the worst case (17 J). As the permanent indentation is well simulated after impact (Fig. 6b), the curve of CAI stress versus indentation also shows a good correlation. This curve is of utmost importance for industry as it gives the residual strength of the plate as a function of damage detectability, which is an essential datum for design choice.

For the stress–deflection curve (Fig. 9), the deflection corresponds to the out-of-plane displacement of the plate center, mainly due to buckling, and measured on both sides of the plate. An LVDT sensor is used on the back face of the plate, and Digital Image Correlation on the impact face. These two curves show the traditional buckling behavior of impacted plates, increasing with the damage size or impact energy level, even if it is overestimated in simulations. The 29.5 J test curve clearly shows a difference in deflection between the two faces of the plate, both for the test and the calculation. This is due to the local buckling of parts of delaminated plies as visible on Fig. 7. The displacement obtained on the impacted face is close to the experimental one. However, displacement of the back face is overestimated, due to an excessive buckling of delaminated plies. For the 6.5 J impact (test and modeling), deflections on both faces are the same, due to the slight damage induced by this impact energy level.

We focused on the 29.5 J test for the analysis of rupture mode in the plate. A comparison between the experimental and numerical CAI tests after the 29.5 J impact is shown in Fig. 11. The shape of the plate (impacted side only) is given in Fig. 11a for three different steps of loading during CAI. It shows a relatively good correlation between experiment and model. The longitudinal strain field (x direction) is drawn in Fig. 11c for different levels of load. The experimental field is obtained thanks to two CCD cameras and 3D digital image correlation. As the reference image for digital image correlation is the image taken at the beginning of the CAI test, the field represented here does not take into account the real strains: all strains are equal to zero after impact, and only the additional strains due to CAI are calculated. As for numerical strain, two different fields are plotted: the "real strain", which represents strains both from impact and CAI tests, and the "virtual strain", which only represents the additional strain due to CAI. The "virtual strain" is computed from the "real strain" by subtracting the strain field obtained after impact. The "virtual strain" is displayed in order to compare it with the corresponding experimental strain field. The "real strain" is displayed because it is the field that enables us to determine where failure strains are reached in the plate. The strain scale is the same for experiment and simulation. It is chosen to obtain the color red for positive or null strain, and the color purple for strains which are less than or equal to compression failure strain of T700/M21 ($\varepsilon_0^c = -0.0125$).

The stress-displacement curve (Fig. 11b) shows that the modeling well simulates the experiment, until experimental failure. However, after this point, the final failure numerically obtained is not sharp enough. The final failure is due to the propagation of the compression failure crack in the first ply (0°) in the y direction. As mentioned earlier, the value for G_I^c is artificially low compared to data from literature, but test analyses still do not enable us to determine whether the crack in CAI tests is due to pure compressive failure or more complex failure. Nevertheless, the ultimate stress is well predicted because the additional stress during failure propagation is very weak. This propagation is clearly visible on the numerical strain fields (expansion of the color purple), and also seen on the strain fields experimentally obtained, even if it seems faster (between about −110 and −146 MPa). Fig. 12 shows the "visible to the naked eye" crack from experiment, and the numerical one at 146 MPa. On the model, only one row of elements in the first ply is damaged in compression, and it is the propagation of the compression fiber failure crack already visible after impact (Fig. 7).

It is important to mention that the buckling of the plate and the propagation of the compression crack are linked. Fig. 13 shows the evolution of the crack length with the CAI stress. It is clear that the crack propagates when the plate is saturated in stress, which corresponds to the plateau on the CAI stress – deflection curve (Fig. 9, right). The rupture scenario during CAI testing, when an initial crack is observed after impact, is thus as follows:

- CAI stress increases until buckling appears.
- When there is enough deflection due to buckling or enough stress concentration to lead to failure strain at the tip of the 0° upper ply crack, the latter propagates (imposed strain loading). In this study, propagation is quite stable until the end of the simulation. It is not the case in experiments, where cracks become unstable at an earlier stage.

The failure in CAI is thus due to a coupling between the buckling and the 0° upper ply crack strength. The reason why the crack propagation is more progressive in the model is not obvious. Three parameters can have an influence: – the fact that the initial crack, induced by the impact, is overestimated by the model; – the fact that, in reality, the crack propagation mode is maybe more complex than the pure compression failure model, with a part of shear-driven compression failure; – and the uncertainties in the mechanical properties used to rule the compressive failure in fiber direction. It should also be noted that there could be dispersion in the experimental test results, but no repeatability tests were performed during this test campaign to enlarge the database.

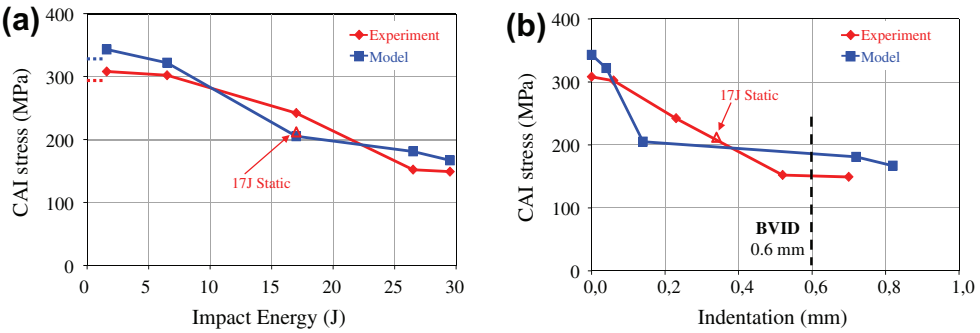

Fig. 10. CAI strength versus impact energy (a) and indentation (b) numerically and experimentally obtained. (For interpretation of the references to color in this figure legend, the reader is referred to the web version of this article.)

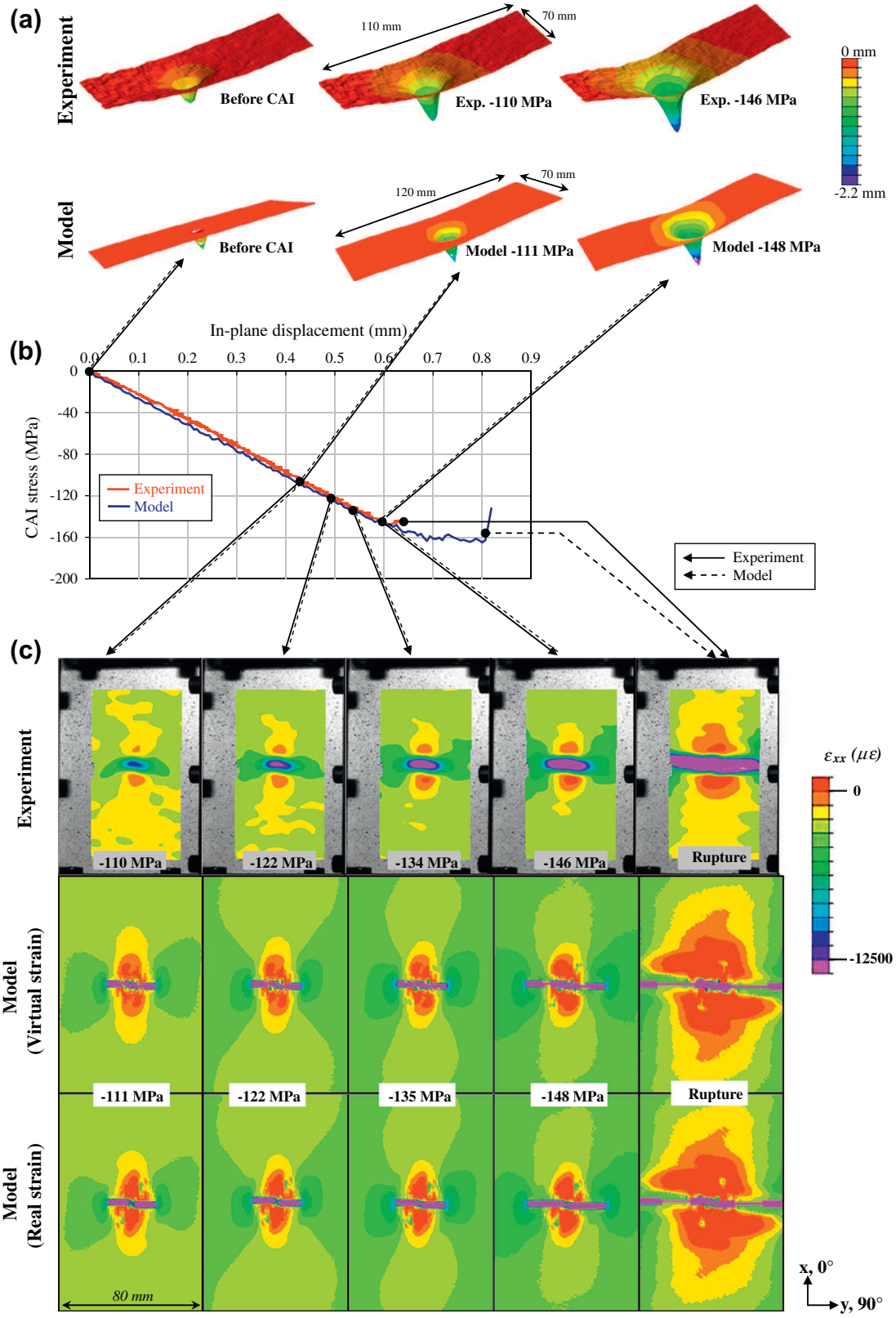

Fig. 11. CAI after a 29.5 J impact: (a) deformed shape of the plate, (b) stress/displacement curve and (c) longitudinal strain fields. (For interpretation of the references to color in this figure legend, the reader is referred to the web version of this article.)

For lower energies, the scenario is not the same. In simulation, 1.6 J impact led to CAI failure at the tip of the plate, as during experiments. For 6.5 J impact simulation, no crack is visible around the impact area after impact. Then, during CAI, deflection is low and rupture suddenly appears, but not around the place of impact. The CAI rupture stress versus impact energy curves from model and experiment (Fig. 10) show that, for these two lower energy impacts, CAI strength is quite high and then decreases before the

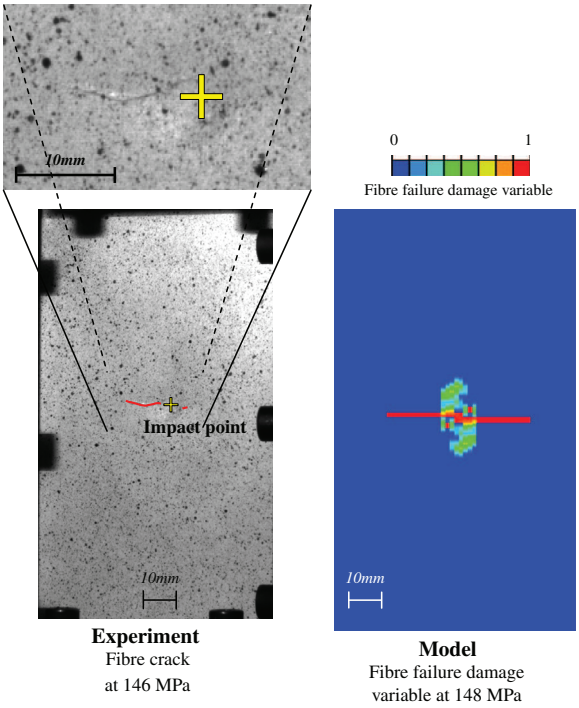

Fig. 12. Experimental and numerical cracks during CAI test (impact test at 29.5 J). (For interpretation of the references to color in this figure legend, the reader is referred to the web version of this article.)

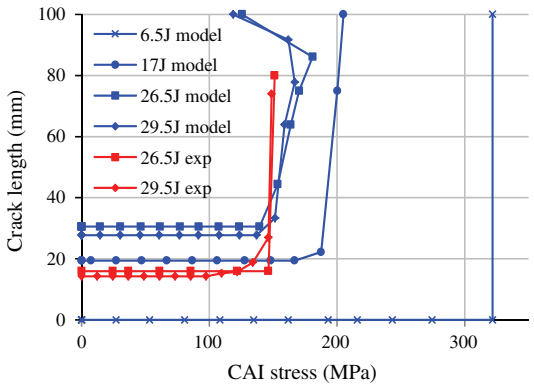

Fig. 13. Evolution of crack length during CAI simulations. (For interpretation of the references to color in this figure legend, the reader is referred to the web version of this article.)

17 J impact test. For 17 J tests, no crack can be observed around the impact area just after impact but the rupture in CAI is due to an unstable crack propagating from the impact area to the edges of the plate. This propagation is not represented in Fig. 13, as it happens suddenly.

It seems that in the studied laminate, the decrease in strength of the plate is due to the change in rupture mode: the presence of the initial crack at the end of the impact leads to rupture by propagation of the crack in the buckled plate, whereas rupture is sudden (no stable propagation of cracks) when no crack is observed.

4. Conclusion

A single model enabling us to simulate both impact and CAI tests on composite laminated plates has been elaborated. Its ability to simulate impact is validated thanks to an experimental – numerical comparison on a given laminate for a wide range of impact energy levels ranging from 0 to 30 J, which is more than the necessary level to reach BVID. As for impact loading, both damage in the plate and permanent indentation are well represented. In particular, the presence of a crack due to fiber failure in compression in the upper ply is simulated, which plays an important role in CAI rupture.

Concerning CAI test simulation, the model accounts for fiber failure crack propagation and local buckling of delaminated areas. It enables the failure scenario during CAI testing to be highlighted and the concurrence of two phenomena – the well-known buckling of the impact damaged area and the propagation of a crack right next to the point of impact. This crack, situated in the upper ply, on the impacted face, is a compression fiber failure crack created during impact which propagates under compression stress during CAI. These two phenomena develop together during CAI and induce final failure of the plate. As the damage is well predicted by the first step (impact) of the calculation, the CAI strength is also well predicted – both qualitatively and quantitatively – for the given range of impact energies.

The fact that the model can predict the appearance and propagation of this crack is of utmost importance, as composite structures are currently designed using the *no-growth* concept in aeronautics.

Finally, as this model allows the permanent indentation after impact and the residual strength to be numerically estimated, it is therefore possible to numerically optimize this plate with impact damage tolerance by changing the stacking sequence within the weight and loading constraints.

References

[1] Abrate S. Impact on composite structures. Cambridge University Press; 1998.
[2] Razi H, Ward SH. Principles for achieving damage tolerant primary composite aircraft structures. In: 11th DoD/FAA/NASA conference on fibrous composites in structural design. Fort Worth, USA; 1996.
[3] Rouchon J. Fatigue and damage tolerance aspects for composite aircraft structures. Delft, 1995.
[4] Alderliesten RC. Damage tolerance of bonded aircraft structures. Int J Fatigue 2009;31:1024–30.
[5] Petit S, Bouvet C, Bergerot A, Barrau JJ. Impact and compression after impact experimental study of a composite laminate with a cork thermal shield. Compos Sci Technol 2007;67:3286–99.
[6] Zheng D, Binienda WK. Effect of permanent indentation on the delamination threshold for small mass impact on plates. Int J Solids Struct 2007;44:8143–58.
[7] Allix O, Blanchard L. Mesomodeling of delamination: towards industrial applications. Compos Sci Technol 2006;66:731–44.
[8] Choi HY, Chang FK. A model for predicting damage in graphite/epoxy laminated composites resulting from low-velocity point impact. J Comput Math 1992;26:2134–69.
[9] Xiong Y, Poon C. A prediction method for the compressive strength of impact damaged composite laminates. Compos Struct 1995;30:357–67.
[10] Naik NK, Ramasimha R. Estimation of compressive strength of delaminated composites. Compos Struct 2001;52:199–204.
[11] Qi B, Herszbergb I. An engineering approach for predicting residual strength of carbon/epoxy laminates after impact and hygrothermal cycling. Compos Struct 1999;47:483–90.
[12] Suemasu H, Sasaki W, Ishikawa T, Aoki Y. A numerical study on compressive behavior of composite plates with multiple circular delaminations considering delamination propagation. Compos Sci Technol 2008;68:2562–7.
[13] De Moura MFSF, Gonçalves JPM, Marques AT, De Castro PMST. Modeling compression failure after low velocity impact on laminated composites using interface elements. J Comput Math 1997;31:1462–79.
[14] Soutis C, Curtis PT. Prediction of the post-impact compressive strength of cfrp laminated composites. Compos Sci Technol 1996;56:677–84.
[15] Habib FA. A new method for evaluating the residual compression strength of composites after impact. Compos Struct 2001;53:309–16.
[16] Hawyes VJ, Curtis PT, Soutis C. Effect of impact damage on the compressive response of composite laminates. Composites Part A 2001;32:1263–70.
[17] Yan H, Oskay C, Krishnan A, Xu LR. Compression-after-impact response of woven fiber-reinforced composites. Compos Sci Technol 2010;70:2128–36.
[18] Zonghong X, Vizzini AJ, Qingru T. On residual compressive strength prediction of composite sandwich panels after low-velocity impact damage. Acta Mech Solida Sin 2006;19:9–17.

[19] Lacy TE, Hwang Y. Numerical modeling of impact-damaged sandwich composites subjected to compression-after-impact loading. Compos Struct 2003;61:115–28.
[20] Davies GAO, Hitchings D, Besant T, Clarke A, Morgan C. Compression after impact strength of composite sandwich panels. Compos Struct 2004;63:1–9.
[21] Aminanda Y, Castanié B, Barrau JJ, Thevenet P. Experimental and numerical study of compression after impact of sandwich structures with metallic skins. Compos Sci Technol 2009;69:50–9.
[22] González EV, Maimí P, Camanho PP, Turon A, Mayugo JA. Simulation of drop-weight impact and compression after impact tests on composite laminates. Compos Struct 2012;94:3364–78.
[23] Falzon BG, Faggiani A. Predicting low-velocity impact damage in stiffened composite panels using high fidelity finite element modelling. In: 14th european conference on composite materials, Budapest, Hungary; 2010.
[24] Bouvet C, Rivallant S, Barrau JJ. Low velocity impact modeling in composite laminates capturing permanent indentation. Compos Sci Technol 2012;72:1977–88.
[25] Bouvet C, Hongkarnjanakul N, Rivallant S, Barrau JJ. Dynamic failure of composite and sandwich structures. In: Abrate S, Castanié B, Rajapakse YDS, editors. Discrete impact modelling of inter- and intra-laminar failure in composites. Springer; 2013 [chapter 8].
[26] Bouvet C, Castanié B, Bizeul M, Barrau JJ. Low velocity impact modelling in laminate composite panels with discrete interface elements. Int J Solids Struct 2009;46:2809–21.
[27] Bazant ZP, Oh BH. Progressive crack and band theory for fracture of concrete. Mater Struct 1983;16:155–77.
[28] Shi Y, Swait T, Soutis C. Modelling damage evolution in composite laminates subjected to low velocity impact. Compos Struct 2012;94:2902–13.
[29] Pinho ST, Robinson P, Iannucci L. Fracture toughness of the tensile and compressive fibre failure modes in laminated composites. Compos Sci Technol 2006;66:2069–79.
[30] Israr HA, Rivallant S, Barrau JJ. Experimental investigation on mean crushing stress characterization of carbon-epoxy plies under compressive crushing mode. Compos Struct 2013;96:357–64.
[31] Faggiani A, Falzon BG. Predicting low-velocity impact damage on a stiffened composite panel. Composites Part A 2010;41:737–49.
[32] Wisnom MR. Modelling discrete failures in composites with interface elements. Composites Part A 2010;41:795–805.
[33] Vogler M, Rolfes R, Camanho PP. Modeling the inelastic deformation and fracture of polymer composites – Part I: plasticity model. Mech Mater 2013;59:50–64.
[34] Vyas GM, Pinho ST, Robinson P. Constitutive modelling of fibre-reinforced composites with unidirectional plies using a plasticity-based approach. Compos Sci Technol 2011;71:1068–74.
[35] Abi Abdallah E, Bouvet C, Rivallant S, Broll B, Barrau JJ. Experimental analysis of damage creation and permanent indentation on highly oriented plates. Compos Sci Technol 2009;69:1238–45.
[36] Airbus Industries Test Method: AITM 1-0010: determination of compression strength after impact.
[37] Aymerich F, Priolo P. Characterization of fracture modes in stitched and unstitched cross-ply laminates subjected to low-velocity impact and compression after impact loading. Int J Impact Eng 2008;35:591–608.
[38] Aktas M, Karakuzu R, Arman Y. Compression after impact behavior of laminated composite plates subjected to low velocity impact in high temperatures. Compos Struct 2009;89:77–82.
[39] Uda N, Ono K, Kunoo K. Compression fatigue failure of CFRP laminates with impact damage. Compos Sci Technol 2009;69:2308–14.
[40] Ghelli D, Minak G. Low velocity impact and compression after impact tests on thin carbon/epoxy laminates. Composites Part B 2011;42:2067–79.